Tsunoda *Progress in Earth and Planetary Science* (2015) 2:9
DOI 10.1186/s40645-015-0038-5

Progress in Earth and Planetary Science
a SpringerOpen Journal

RESEARCH ARTICLE Open Access

Upwelling: a unit of disturbance in equatorial spread *F*

Roland T Tsunoda

Abstract

Plasma structure in the nighttime equatorial *F* layer, often referred to as equatorial spread *F* (ESF), is not uniformly distributed, either in time or in space. Observations indicate that ESF in the bottomside *F* layer takes the form of patches; plasma structure within the *F* layer takes the form of localized plasma depletions, called equatorial plasma bubbles (EPBs), which tend to occur in clusters. Another observed feature is an upwelling, which has been described as a localized, upward modulation of isodensity contours in the bottomside *F* layer. Interestingly, zonal widths of ESF patches, EPB clusters, and upwellings are similar. Moreover, all display an east-west asymmetry. The objective of this paper is to show, for the first time, that an ESF patch is the bottomside counterpart of an EPB cluster, and that both are products of the electrodynamical process that takes place within an upwelling. The process can be described as having three phases: (1) amplification of upwelling amplitude during the post-sunset rise of the *F* layer, (2) launching of the first EPB of the evening, from crest of the upwelling, and (3) structuring of plasma within the upwelling. Hence, an upwelling, whose presence is responsible for the formation of ESF patches and EPB clusters, can be envisioned as a unit of disturbance that occurs in the nighttime equatorial ionosphere.

Keywords: Equatorial spread F; F-region plasma structure; Equatorial ionosphere; Equatorial plasma bubbles; Deep convective activity in troposphere; Atmospheric gravity waves; Neutral-ion coupling; Swoopers; Transequatorial propagation; Interchange instability

Background

Overview

Plasma structure, found in the nighttime equatorial *F* layer, is often referred to as equatorial spread *F* (ESF). Although the term was coined originally to describe the spreading of the *F* trace (in range) in ionograms (Cohen and Bowles, 1961), it is now used generically to refer to both the structure and the conditions that are conducive for its development. Our knowledge and understanding of ESF have evolved from views of structure in the bottomside of the *F* layer with ground-based sensors, and from measurements made *in situ* within the *F* layer with space-borne instruments. Useful and unifying glimpses, though only occasional, have been provided by rockets and incoherent-scatter (IS) radars.

A better understanding of the physical processes is slowly emerging as theoretical and modeling studies are conducted to interpret observations. Clearly, theories and model outputs cannot be properly evaluated without observations that are both comprehensive and accurate. In this regard, we believe that the measurements needed to answer the outstanding questions on ESF are not being made (e.g., see Tsunoda 2005).

In the meantime, we believe that much can be learned by considering whether the 'patchiness' of ESF and the 'clustering' of equatorial plasma bubbles (EPBs) (e.g., McClure et al. 1977) are related, through some kind of physical process. Clearly, if this kind of relationship can be shown to exist, a unified and more comprehensive description of ESF would emerge. Patches have been detected in the bottomside *F* layer, over several decades, with ground-based instruments such as (1) ionosondes (Calvert and Cohen 1961; Cohen and Bowles 1961), (2) radio experiments (Calvert et al. 1963; Davies and Chang 1968; Röttger 1973), and (3) radars (Clemesha 1964; Kelleher and Skinner 1971). Impressions are that the patches, observed by these different methods, are produced by related plasma structures (e.g., Kelleher and Röttger 1973; Aarons et al. 1978). Within the *F* layer, ESF takes the form of EPBs

Correspondence: tsunoda@sri.com
Center for Geospace Studies, SRI International, 333 Ravenswood Ave, Menlo Park, CA 94025, USA

(e.g., Tsunoda 1981; Tsunoda et al. 1982), which are spaced in longitude. A closer examination reveals that EPBs occur more often in clusters (e.g., Singh et al. 1997), than they do individually. Interestingly, other observations have shown that an upwelling (i.e., localized altitude modulation) often appears in the bottomside *F* layer, prior to the development of ESF or EPBs (e.g., Tsunoda and White 1981; Tsunoda 2005). Moreover, the width of an upwelling is very similar to those of ESF patches and EPB clusters. And, there is further evidence that an upwelling can control when, where, and how an ESF patch or EPB cluster develops (Tsunoda and White 1981; Tsunoda 2005).

Methods

Objectives

The objectives of this paper are to unify the observations of ESF and EPBs, and to validate the following hypothesis:

- The formation of ESF patches and EPB clusters is controlled by the electrodynamics that sets up within an upwelling in bottomside of the equatorial *F* layer

An upwelling is defined as a localized, upward displacement of isodensity contours in the bottomside of the *F* layer, as shown in Figure 1 (an upwelling can appear in apparent isolation, at some longitude, or several can appear as a wave train; the latter is referred to as large-scale wave structure (LSWS)). The contours, shown between 300 and 450 km in altitude, describe the distribution of plasma density (*N*). Here, upwelling amplitude is about 50 km and zonal width is about 300 km (the increased jaggedness in contours associated with lower *N* values is produced by low signal-to-noise ratios, and should be ignored for our purposes here). The smattering of small pink islands that appear in the vicinity of 500 km altitude is associated with the peak of the *F* layer. Perhaps the earliest measurement of an upwelling was made with a 630 nm all-sky imager by Weber et al. (1978, 1980, 1982). A collocated ionosonde showed that local uplifting of isodensity contours was associated with the north-south-aligned channel of nightglow depletion. Unambiguous descriptions of this kind are few and far between because they are available only from ALTAIR, a fully steerable incoherent scatter (IS) radar (Tsunoda et al. 1979; Tsunoda and White 1981; Tsunoda 1983). Less-direct results have been obtained from variations in total electron content (TEC) as a function of longitude (e.g., Thampi et al. 2009; Tsunoda et al. 2010); these more routine measurements have shown that occurrences of upwellings are fairly common (Tulasi Ram et al. 2014).

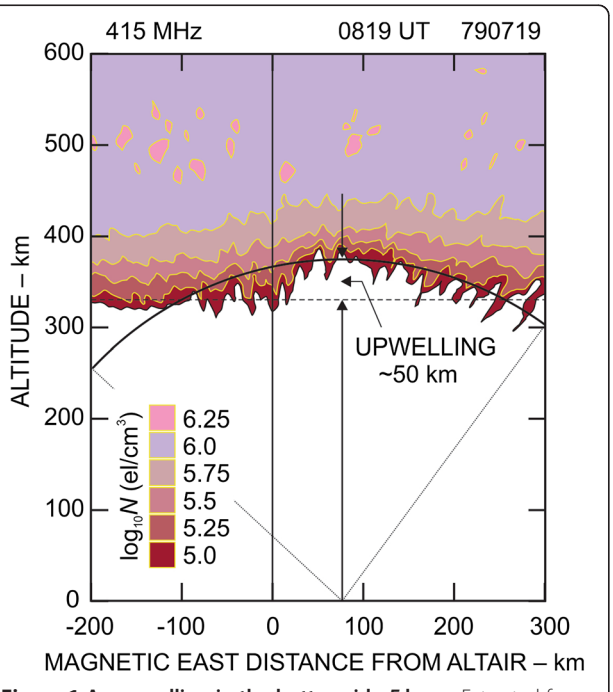

Figure 1 An upwelling in the bottomside *F* layer. Extracted from ALTAIR IS measurements made at 0819 UT on 19 July 1979.

In the remainder of this paper, we show how an upwelling provides the framework for the development of (1) each patch that is detected by a ground-based sensor, and (2) each cluster of EPBs that is encountered by a satellite-borne instrument. We conclude that an upwelling can be viewed as a unit of disturbance in ESF. To place this kind of description in context, we note that usage of the term 'convective ionospheric storm' to refer to ESF has increased (e.g., Makela et al. 2005, 2006; Kelley et al. 2005, 2009, 2011). If the research community chooses to accept this terminology, it may be reasonable to refer to the process, which takes place within an upwelling, as a convective ionospheric substorm.

ESF patches in bottomside *F* layer

The properties of ESF patches found in the bottomside of the equatorial *F* layer, presented below, have been compiled from (1) bistatic radio propagation experiments, in which both the Doppler shift and spread in a continuous-wave (CW) signal were measured; (2) transequatorial propagation (TEP) experiments, in which the delay and azimuthal angle-of-arrival of pulsed transmissions were measured; and (3) ionograms, which were recorded at a station near the magnetic dip equator. We show that, regardless of the method of measurement, ESF patches appear sequentially, starting around the end of the post-sunset rise (PSSR) of the *F* layer, and each patch displays an east-west (EW) asymmetry.

Results

Radio propagation: CW-DOPPLER results

Indications that ESF consists of drifting patches of plasma structure first appeared in radio propagation experiments, which were conducted in Africa during the early 1960s. A radio link was set up from Tripoli, Lybia (32.5° N, 13.1° E) to Accra, Ghana (5.3° N, 0.2° W) (Calvert et al. 1963); later, another link was set up from Monrovia, Liberia (6.2° N, 10.5° W) to Accra (Davies and Chang 1968). In both experiments, a CW signal was transmitted from one location, and Doppler properties of the received signal were monitored at the other. The baseline of the Monrovia-Accra path was about 1,175 km long and aligned east-southeastward from the magnetic dip equator (Davies and Barghausen 1966). The baseline of the Tripoli-Accra path was 3,315 km long and aligned south-southwestward from the magnetic meridian (these baselines can be compared with those used for TEP experiments, in 'Transequatorial propagation results' section).

The patchy nature of signals received at Accra from Monrovia, on 26 to 27 October 1963, can be seen in Figure 2, which is reproduced from Davies and Chang (1968) with added notation. The signal of interest can be seen to have had essentially a zero Doppler shift at 1600 universal time (UT). We interpret this behavior to be associated with a propagation path that underwent a one-hop reflection from the bottomside of a stationary, and horizontally stratified, *F* layer. The Doppler shift of this trace became increasingly more negative during the PSSR of the *F* layer, and reached a maximum value around 1830 UT (indicated by a downward-pointing red arrow), which is close to *E*-region sunset (SS_E). The spreading of the trace indicates the presence of ESF. After 1940 UT, three somewhat spread traces appeared in sequence; all displayed a large positive Doppler shift, which decreased with time. Each of these traces was referred to as a 'swooper' (Davies and Chang 1968). The Doppler shifts of the first two swoopers changed sign, but their magnitudes did not approach those, when the sign was positive. The Doppler shift of the third swooper approached zero and remained small in magnitude. This Doppler signature is a good example of the EW asymmetry, which is a distinctive property of ESF patches (e.g., Röttger 1973; Maruyama and Kawamura 2006) and EPB clusters.

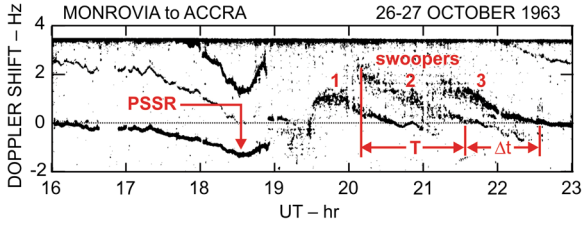

Figure 2 An example of swoopers, detected by a CW-Doppler technique, along the Monrovia-Accra path on 26 to 27 October 1963. Reproduced from Davies and Chang (1968) with added notation.

The finding that two swoopers can coexist at any given time, separated by different Doppler shifts, is also direct evidence that these structures were spatially separated in longitude (that is, different Doppler shifts would be measured, if signals arrive from different longitudes at different elevation angles). In this regard, Davies and Chang (1968) found that only one swooper was usually detected on a given night, although there were a few nights when up to five swoopers were detected. The duration of a swooper varied between 30 min and 2 h; typical duration was 1 h. Similarly, the spacing between two swoopers was also about an hour. We should keep in mind, however, that these properties are colored by the transport velocity of patches and the reflection geometry of the experiments.

Transequatorial propagation results

A more global view of patches is available from TEP experiments, in which both transmitter and receiver are located at substantial distances from the dip equator (e.g., see review of TEP by Nielson and Crochet 1974). For example, the lengths of great-circle TEP paths (1) from Tsumeb (19.3° S, 17.7° E) to Lindau (51.4° N, 10.1° E) (Röttger 1973), and (2) from Shepparton (36.2° S, 135.3° E) to Oarai (36.3° N, 140.6° E) (Maruyama and Kawamura 2006; Saito et al. 2008), were both about 8,000 km. With this viewing geometry, signals that arrive at azimuths ±60° away from the great-circle path have been detected.

Patches were found to first appear around the end of the PSSR (Maruyama and Kawamura 2006), and become distributed, sometimes over 10,000 km in EW extent (Röttger 1973). These propagation modes have been interpreted in terms of side reflections from tilted plasma structures, near the magnetic dip equator, that are aligned with geomagnetic field (*B*) lines. One to six (and as many as ten) patches have been observed simultaneously during an interval of 15 min. The lifetime of a patch could vary between 15 and 120 min, which is essentially the same as that of a swooper. The spacing between patches could be less than 100 km or more than 1,500 km; the median value was 380 km (Röttger 1973). Allowing zonal transport, the typical spacing between swoopers is also about 400 km, which is in excellent agreement with patch separation (for example, nine patches spaced 400 km in longitude, would span 3,200 km, or about 2 h in local time). The median eastward drift speed was found to be 110 m/s (Röttger 1973).

Results from TEP also contained an EW asymmetry, which is reminiscent of that found in swoopers. That is, patches from the Tsumeb-Lindau experiment were observed more often in the sector to the west of the great-

circle path, than observed in the sector to the east; the ratio of west-to-east occurrences was a factor of two in the results reported by Röttger (1973). Patches from the Shepparton-Oarai experiment were predominantly from the west sector for the month of March, 2003, according to Maruyama and Kawamura (2006).

Digisonde results

Features found in equatorial ionograms are also consistent with those found in swoopers and TEP patches; that is, range spread *F* (RSF) is also patchy, approaches from the west and recedes to the east, while displaying an EW asymmetry. To illustrate, we have scaled ionograms obtained with a Digisonde at Jicamarca, Peru (11.95° S, 76.87° W), and constructed a family of virtual height (*h*') curves versus UT, which is presented in Figure 3. Each curve is associated with an integer value of the plasma frequency, from 3 to 8 MHz (as labeled near the left ordinate). We have also plotted the minimum virtual height of the bottomside *F* layer (*h*'*F*), which is shown as a gray curve. The times for SS_E and sunset in the *F* region (SS_F) are marked with vertical gray lines. From these curves, we can recognize the PSSR of the equatorial *F* layer, which occurred between 2300 and 0030 UT, and its descent, between 0130 and 0400 UT.

Of interest is the altitude modulation found in the *h*'(3 MHz) curve, and the development and distribution of RSF. A maximum in *h*'(3 MHz) occurred around 0130 UT, accompanied by some RSF at 3 MHz. Thereafter,

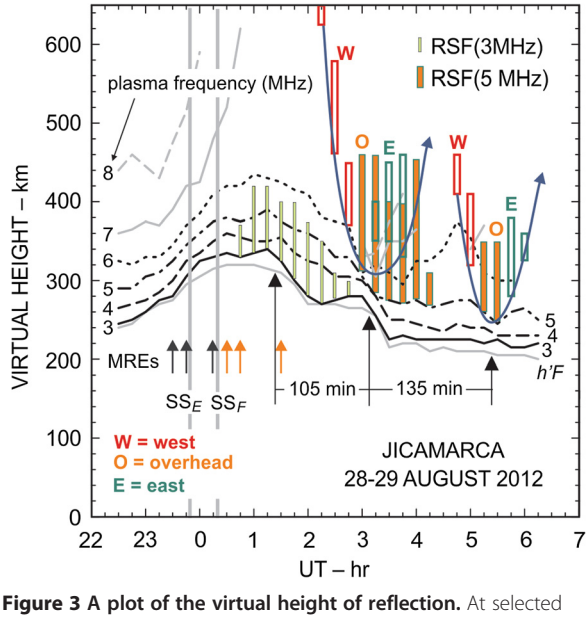

Figure 3 A plot of the virtual height of reflection. At selected ionosonde frequencies, presented as a function of UT on 28 to 29 August 2012. Also included are occurrence times for SS_E and SS_F, and MREs. Vertical bars indicate the times and virtual heights over which RSF was observed.

the *h*'(3 MHz) trace decreased rapidly and reached a minimum value around 0220 UT; the continued presence of RSF (3 MHz) suggests that it occurred more or less from the overhead direction. The *h*'(3 MHz) trace appeared to rise slightly, reaching a relative maximum around 0325 UT. This maximum was accompanied by oblique RSF (5 MHz) traces, which were first seen at earlier times, to the west of Jicamarca (from angle-of-arrival determination). When *h*'(3 MHz) reached its maximum, the RSF appeared to be coming from overhead, together with stronger RSF (5 MHz). As the *h*'(3 MHz) curve started to decrease again, we see that RSF (5 MHz) became stronger, and there was a component of RSF (3 MHz) that came from the east.

The EW asymmetry is evident from the fact that RSF (3 MHz) did not reach virtual heights as 'high' to the east, as they did when RSF was first detected to the west. We suggest that the source of this asymmetry is closely related to those seen in swoopers and TEP measurements. A similar pattern in RSF can be seen in Figure 3, between 0500 and 0600 UT, but there is almost no evidence of modulation in the *h*'(3 MHz) curve. The reason for this behavior is likely that the bottomside of *F* layer had reached altitudes, where chemical recombination, not plasma transport, controls the altitude profile of *N*. Moreover, the amplitude of upwellings decreases during the descent of the *F* layer, for the same reason that it increases during the PSSR. In any case, the presence of RSF with this familiar distribution suggests that another patch had passed over the Digisonde at Jicamarca. Hence, the evidence suggests that there were three upwellings that developed on this night, which became 'filled' with ESF.

EPB clusters in *F* layer

Our hypothesis, that EPBs develop within the confines of an upwelling, was actually formulated from the results obtained with ALTAIR, a fully-steerable IS radar (Tsunoda et al. 1979; Tsunoda and White 1981; Tsunoda 1983). Similar conclusions can be drawn from *in situ* measurements made from the Atmospheric Explorer *E* (AE-E) satellite (Singh et al. 1997). A clear example of LSWS with associated upwellings (first pass), which become filled with localized depletions (second pass), is presented in Figure 4; this plot is from Singh et al. (1997) with added notation. This event occurred on 30 March 1977, when AE-E was in a circular orbit at an altitude of 275 km. The ion number density (N_i), measured with an ion-drift meter onboard AE-E during two consecutive orbits, 7192 and 7193, is shown with two traces. Three upwellings (marked by downward-pointing arrows) are clearly evident in the upper trace, from orbit 7192. In comparison, the N_i values in this example are between 10^5 and 10^6 ions/cm^3, which are similar to those associated with the upwelling in

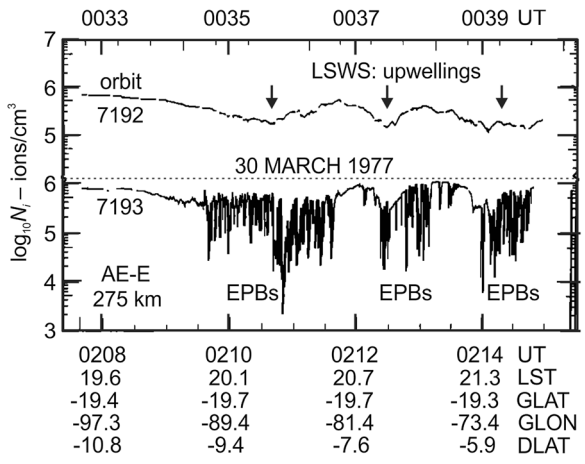

Figure 4 Upwellings measured by the AE-E satellite during one pass, and clusters of EPBs during the next pass. This figure, without annotations, is from Singh et al. (1997).

Figure 1. The UT scale associated with that orbit is shown along the top of the plot. During orbit 7193, considerable structure was present, as seen in the lower trace. The UT scale, together with those for local solar time (LST), geographic latitude (GLAT), geographic longitude (GLON), and magnetic dip latitude (DLAT), are shown along the bottom of the plot. The dotted line indicates where there is a break in the scale for N_i, along the ordinate. Although we have listed GLAT or GLON for orbit 7192, the trajectories were separated by no more than 2° in GLAT near the west end of the LSWS, so that orbit 7193 was essentially collocated with orbit 7192 near the east end of the LSWS. Hence, there is no doubt that the structure developed within upwellings, during the time between the two orbits.

There are several features of interest in Figure 4. The first is the encounter of LSWS, which occurred around 0035 UT, where GLON was 90° W. At this longitude, LST lags UT by 6 h, which means local time was approximately 1835 LST, when the solar zenith angle was about 98.5°, which corresponds with a time just before SS_E. This finding is consistent with earlier results, which showed that LSWS can be detected as early as in the late afternoon (Thampi et al. 2009; Tsunoda et al. 2011, 2013), and is amplified during the PSSR of the *F* layer (Tsunoda and White 1981; Tsunoda et al. 2013). Note that the upper envelope of N_i, which tracks the quiet regions and the maxima of the structure, resembles the modulation of the trace from the first pass. Hence, each cluster of plasma structure can be interpreted as localized depletions in N_i that developed within an upwelling. Stated another way, each upwelling appears to become filled with EPBs. Other examples from AE-E results can be seen in Hysell and Kelley (1997), their Figure 1; Kil and Heelis (1998a), their Figures 2 and 6; Kil and Heelis (1998b), their Figures 2 and 9; and Hei et al. (2005), their Figures 1 and 2.

Upwelling control: three phases

The development of ESF and EPBs can be described in terms of three phases: growth, onset, and structure. During the growth phase ('Growth phase: amplification of upwellings' section), which takes place during the PSSR, upwelling amplitude is amplified. During the onset phase ('Onset phase: ESF patches and primary EPBs' section), which takes place around the end of the PSSR, the first EPB of the evening is observed. And, during structure cluster phase ('Structure phase: clustering and EW asymmetry' section), which takes place during the descent of the *F* layer, plasma structure develops within each upwelling, in the form of ESF patches and EPB clusters. Evidence of this upwelling control is described below. Discussion and interpretation of key findings are presented in 'A working model' section.

Growth phase: amplification of upwellings

Amplification

ALTAIR IS measurements have provided direct evidence that upwellings are amplified during PSSR (Tsunoda and White 1981). Less-direct results have been obtained by examining the variations in TEC as a function of longitude. That is, signals from the CERTO radio beacon (Bernhardt and Siefring 2006) on the Communication/Navigation Outage Forecasting System (C/NOFS) satellite (De la Beaujardiere et al. 2004), in a low-inclination orbit, were recorded at ground stations; TEC was estimated using the differential-phase technique (e.g., Thampi et al. 2009; Tsunoda et al. 2010; Tulasi Ram et al. 2012). Variations in TEC with longitude were interpreted in terms of LSWS in the bottomside *F* layer (Tsunoda et al. 2013), and the results from successive satellite passes have shown that upwelling amplitude does grow during the PSSR (Tsunoda et al. 2010, 2013).

Ionogram signatures

Additional evidence regarding upwelling presence comes from two ionogram signatures, namely multi-reflected echoes (MREs) (Tsunoda 2009; Thampi et al. 2012; Tsunoda et al. 2013) and satellite traces (STs) (Abdu et al. 1981; Tsunoda 2008; Thampi et al. 2012). The finding that MREs appear most often around the time of SS_E (Tsunoda et al. 2015) is consistent with the finding that upwellings are amplified during the PSSR; in fact, the maximum in PSSR rate is centered more or less about SS_E (Tsunoda 2009; Tsunoda et al. 2015). Occurrences of MREs, in Figure 3, are marked with short, upward-pointing arrows. Most were detected during the PSSR (when isodensity contours are sloped upward, from west to the east). Typically, MREs appear first, especially around SS_E, followed

by STs (e.g., see Tsunoda et al. (2013), their Figure 1). Both have been referred to as precursors because they precede the development of ESF.

The MREs are produced by multiple ionospheric reflections, which are indicative of an enhancement in reflection coefficient. Enhancement is possible, when reflection occurs from concave isodensity contours, such as those associated with an upwelling (Tsunoda 2009; Thampi et al. 2012). Enhancement should be strongest, when the radius of curvature of the reflecting surface is approximately equal to the height of reflection. We can see that this is the case for the upwelling shown in Figure 1, where we have scribed a circular arc for comparison. Hence, it should be apparent that the zonal wavelength of an LSWS would be about 300 km, when MREs are observed. And, indeed, the median patch size, from TEP experiments, is 380 km (Röttger 1973). Estimates of patch size or spacing, by other means, are also about 400 km (Aarons et al. 1978; Tsunoda and White 1981).

An ST appears to involve an oblique propagation path with reflection from a tilted isodensity surface (e.g., a wall of an upwelling). If the tilt of the reflection surface is slight, the propagation path back to the ionosonde could involve two ionospheric reflections and one ground reflection. In this case, the ST would appear offset from the two-hop (2 *F*) trace (Tsunoda 2008), which is assumed to be produced by two overhead reflections from a horizontally stratified *F* layer. In fact, an ST associated with the 2 *F* trace often precedes an ST associated with the main one-hop (1 *F*) *F* trace; either or both typically precede the appearance of ESF. The ST associated with the 1 *F* trace involves direct reflection from a more steeply tilted surface. If the shape of the isodensity contours in Figure 1 is typical, an ST could be associated with the 2 *F* trace, if an ionospheric reflection that supports a returning signal occurs from the east wall. Or, an ST could be associated with the 1 *F* trace, if a returning signal occurs from a more steeply inclined west wall.

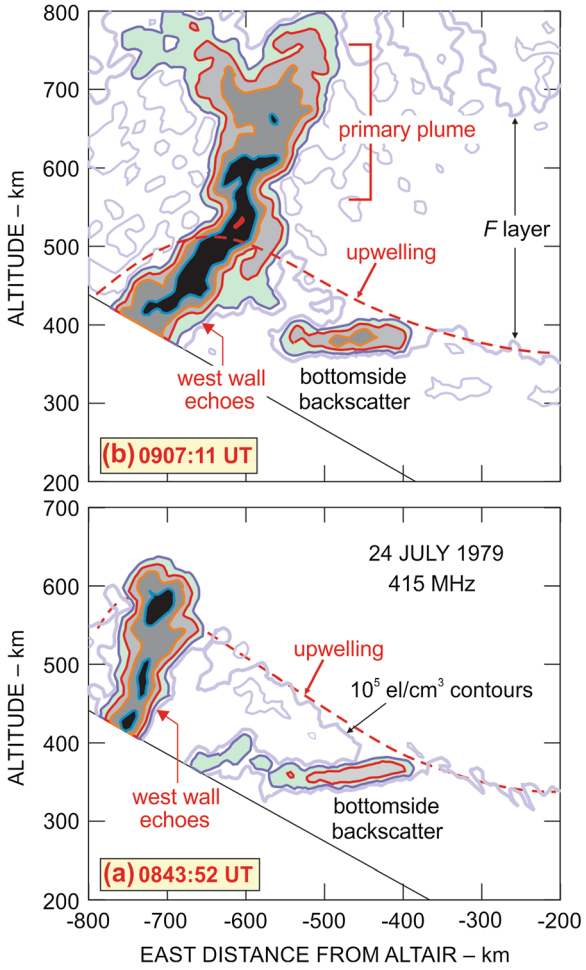

Figure 5 ALTAIR maps showing the radar backscatter. (a) ALTAIR map, which shows that radar backscatter from west wall was present prior to appearance of primary and secondary EPBs. **(b)** ALTAIR map showing the launching of the primary EPB from the crest of the upwelling.

Small-scale irregularities along west wall

A remaining feature, found to occur during growth phase, is radar backscatter from the west wall of an upwelling (Tsunoda 1981, his Figure 3). To illustrate, we present two maps in Figure 5; they were constructed from ALTAIR measurements made on 24 July 1979 (they are replicas of the west upwelling in Tsunoda and White (1981), with added notation). The nominal shape of the upwelling is sketched as a dashed red curve in Figure 5a,b (the purple curve represents the 10^5 el/cm^3 isodensity contour). A tilted echoing region is more or less aligned with the west wall of the upwelling. Hence, this tilted structure can be considered to be a radar signature indicating the presence of an upwelling. An enhancement in amplitude scintillations (produced by km-scale irregularities in *N*) has also been observed along the west wall of an upwelling (Tsunoda et al. 2011; Tulasi Ram et al. 2012). If this plot is typical, we can claim that small-scale irregularities (<1 km) are excited along the west wall during the growth phase, prior to the development of any EPBs. We will return to the difference between west-wall echoes and EPBs in 'Onset phase: ESF patches and primary EPBs' and 'Structure phase: clustering and EW asymmetry' sections.

Onset phase: ESF patches and primary EPBs

The onset phase takes place around the end of the PSSR. During this phase, observations in the bottomside *F* layer indicate the onset of RSF is preceded by appearances of MREs and STs (Tsunoda et al. 2013), as can be seen in Figure 3. First appearance of swoopers also occurs during this phase, as can be seen in Figure 2. Both of these bottomside signatures of ESF patches appear at

the end of the PSSR (notice that MREs and STs, which appear during the growth phase, have relatively discrete traces and are considered to be precursors of RSF and EPBs). A sketch, that shows the nominal onset time for ESF to be around the end of the PSSR, can be found in Clemesha and Wright (1966).

And, observations in the topside *F* layer, during this phase, include the launching of the first (primary) EPB of the evening (Tsunoda 1981; Yokoyama et al. 2004). The appearance of the primary EPB is noteworthy because EPBs are generally absent during the growth phase, which precedes the onset phase. If EPBs are suppressed during the growth phase, an implication is that the process for EPB generation becomes active during the onset phase. We should note that the launching of the primary EPB occurs from near the crest of the upwelling, that is closest to the end of the PSSR (e.g., Tsunoda and White 1981), rather than envisioning the timing of the launch to be associated with the end of the PSSR.

From our perspective, the concavity in isodensity contours plays a central role in EPB production. Concavity is associated with the PSSR and descent of the *F* layer, and also with LSWS amplitude and zonal wavelength. For example, assume that the PSSR rate is 50 m/s and its duration is an hour; if we allow a symmetrical descent of the *F* layer, we will have concave isodensity contours that have a radius of curvature of about 15,000 km. Although curvature appears small, the contours are higher by about 100 km at the end of the PSSR, than they were before the start of the PSSR. Hence, the ion-neutral collision frequency (ν_{in}) is smallest during onset phase, and the linear growth rate of the interchange instability (driven by gravity) (Dungey 1956) reaches a maximum. The conditions are even more favorable for the launching of an EPB, if we include LSWS. Indeed, whereas the PSSR may raise the *F* layer by 100 km, the local altitude modulation associated with an upwelling could easily add another 50 km (see Figure 1). The finding that ESF is associated with a high *F* layer (e.g., Farley et al. 1970) is consistent with the launching of primary EPBs during the onset phase.

Structure phase: clustering and EW asymmetry

Patches and clusters develop during the descent of the *F* layer. During descent, *E* is westward which means the bottomside of a horizontally stratified *F* layer is stable to the interchange process, unless it is high enough in altitude that gravity is the dominant driver. In either case, patches or clusters would not form. On the other hand, the west wall of an upwelling would be unstable to the interchange process, driven by an eastward *U* (Tsunoda 1983). The elements of this process have already been outlined in several papers; we revisit the more important details.

We have already shown how small-scale irregularities appear along the west wall (Tsunoda 1981; Tsunoda et al. 2011) during the growth phase ('Growth phase: amplification of upwellings' section). We also know that the west wall continues to structure, leading to the appearance of secondary EPBs along that wall (Tsunoda 1983). We have not yet paid much attention, however, to the order in which west-wall echoes and EPBs appear. It turns out that this order provides some clues regarding the underlying physics. We found, from Figure 5a, that west-wall echoes precede EPB development (other maps, from this night, can be found in Tsunoda and White (1981). Indeed, if we now refer to Figure 5b, we can see that a primary EPB (plume) developed from the crest of the upwelling, shortly after appearance of the west-wall echoes. We further note that the shape of the west-wall echoes is relatively smooth, indicating that secondary EPBs have not yet formed.

Next, we revisit the ALTAIR backscatter maps in Tsunoda (1983) to examine in more detail how EPB clusters form. To do so, we have constructed a montage of backscatter maps from 24 July 1979, to highlight the temporal development and evolution of the upwelling and the EPBs. The montage is presented in Figure 6 (details of the ALTAIR scans used to construct the montage are given in Table 1). Two backscatter maps are shown in the center panel, positioned according to the magnetic east distance from ALTAIR (at the times the maps were taken). The one on the left, taken at 0907 UT, is essentially that presented in Figure 5b. The approximate shape and location of the upwelling is sketched with a thin red curve. Although the sketch is based simply on the notion that the backscatter must have occurred from a region of steep westward gradient in *N*, and is highly subjective, we believe it is adequate for showing the location of the primary plume (EPB) relative to the upwelling. Referring back to Figure 6, we have shown the nominal location and shape of the primary plume with a thick red curve, which extends upward from the crest of the upwelling. The plot on the right, taken at 1027 UT, 1 h and 20 min after the first, is much more complex than the first.

The temporal evolution of the primary plume and upwelling was tracked by examining four other backscatter maps that were taken between these two. We have included two of the four backscatter maps, one taken at 0927 UT (top panel) and the other at 0958 UT (bottom panel). The map in the top panel shows how structuring along the west wall has grown, from a simple, tilted echo region to a broader distribution with small protrusions. We are also left with the impression that the primary plume has shifted a bit to the east of center. The map in the bottom panel shows how the protrusions have grown along the west wall, and seemingly, the primary plume

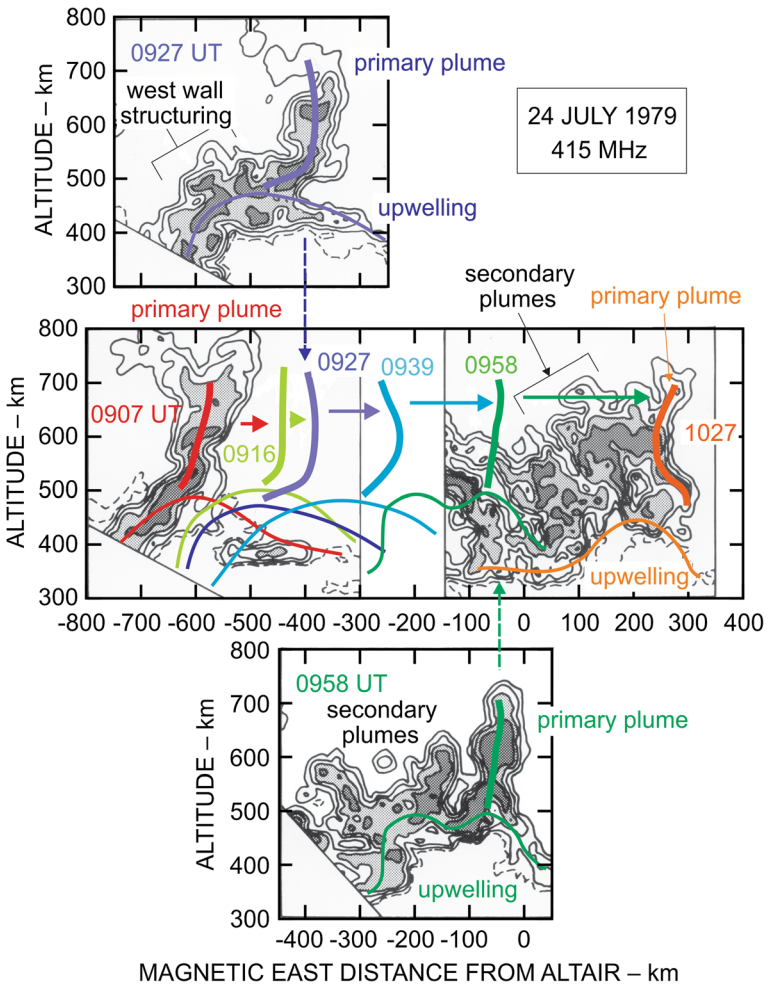

Figure 6 Montage illustration. A montage to illustrate the appearance of primary plume at crest of upwelling (0907 UT), the structuring of the west wall of upwelling (0927 UT), the development of secondary plumes (0958, 1027 UT), and the relative displacement of the primary plume to the eastern edge of the upwelling (1027 UT). Colored curves in the center panel represent the nominal locations of the primary plume and the upwelling, at different times on the night of 24 July 1979. All six of the backscatter maps are shown in Tsunoda (1983).

has moved even further to the east relative to the crest of the upwelling. All positions of the primary plume and upwelling are shown by colored curve segments, which are labeled by the times of maps. The interpretation that the plasma structures along the west wall are secondary plumes, should be evident from the map taken at 1035 UT, which is presented in Figure 7.

It is important to note that both the primary and secondary EPBs appear to be transported eastward relative to the position of the upwelling. The EPBs eventually encroach into the region that was occupied originally by the east wall of the upwelling. A consequence of this encroachment appears to be a steepening of the tilt of the east wall, as the primary plume approaches the eastern boundary of the upwelling. This near alignment of the primary plume with the east wall appears to be a common feature, as seen in other ALTAIR maps (e.g., Tsunoda et al. 1982). This appears to be the process by which the entire upwelling becomes filled with plasma structure. This filling of the upwelling region is consistent with the EPB distribution in the AE-E measurements presented in Figure 4. A discussion of why this

Table 1 ALTAIR scans on 24 July 1979

Scan number	Start and stop times (UT)	Direction (rate)
1	0907:11 - 0915:25	W → E(M*)
2	0915:59 - 0924:11	E → W(M)
3	0926:46 - 0931:36	W → E(M)
4	0939:16 - 0944:06	W → E(M)
5	0957:33 - 0959:25	W → E(F*)
6	1026:41 - 1030:55	E → W(F)
7	1035:53 - 1040:09	E → W(F)

*Scan rates: $M = 0.25°/s$; $F = 0.5°/s$.

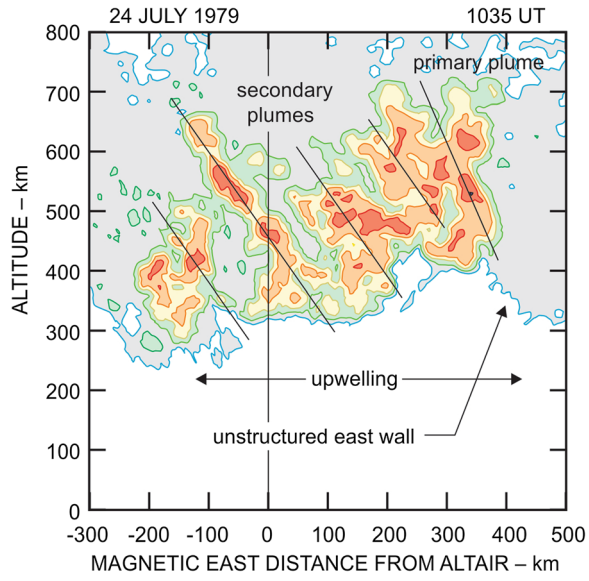

Figure 7 Backscatter distribution obtained with a spatial scan taken at 1035 UT, which clearly shows the cluster of EPBs.

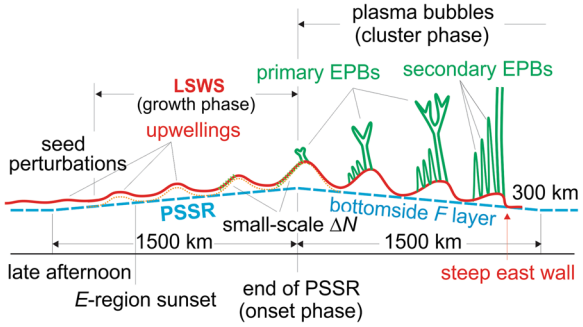

Figure 8 Working hypothesis for the temporal evolution of upwellings and EPBs, from late afternoon to the post-midnight sector.

should happen is presented in 'A working model' section. The process, by which structure develops on the west wall and is transported to the region of the east wall, is clearly susceptible to the development of EW asymmetries.

Discussion

A working model

We believe the evidence supporting the upwelling hypothesis ('Objectives' section) is strong enough to be used as a working model for the development of ESF. Theory, observations, and outputs from computer models can be used to test the robustness of the hypothesis. A sketch that captures the basic elements of this working model is presented in Figure 8. It can be viewed as a snapshot in UT, in which the ordinate is altitude and the abscissa is longitude; the vertical plane is aligned with the magnetic dip equator. The blue dashed line represents an isodensity contour in the bottomside of the *F* layer (the sketch is centered on the end of the PSSR). At the west end of the sketch, LT is assumed to be the late afternoon sector, where small-amplitude LSWS can be present prior to the growth phase ('Growth phase: amplification of upwellings' section). The wavy red curve represents an isodensity contour, when LSWS is present. Although LSWS is shown in Figure 8 to extend without interruption from late sunset to midnight (or later), upwellings can appear in apparent isolation, or in a group of up to ten upwellings (Röttger 1973). In this sketch, the PSSR is shown to take place in 1 h, which is equivalent to about 1,500 km in zonal distance. The distance between upwellings (i.e., wavelength of LSWS) is about 400 km (e.g., Röttger 1973; Tsunoda and White 1981). Sizes of observed patches are also about 400 km (e.g., Aarons et al. 1978).

Convective activity

The source of LSWS remains to be identified. However, the finding that LSWS can appear in the late afternoon suggests that velocity shear, driven by the *F*-region dynamo (Guzdar et al. 1982, 1983), is not the primary source. Instead, we suggest, for our working model, that a more viable source may exist in the lower atmosphere. A popular notion is that a localized region of deep convective activity in the troposphere, referred to as a mesoscale convective complex (MCC), will generate atmospheric gravity waves (AGWs). Conceptually, AGWs could reach the lower thermosphere and produce a polarization *E* in the *E* region, which could map along *B* lines to the base of the *F* layer (the small-amplitude LSWS, found in the late afternoon sector, could be produced in this manner). The smallness of LSWS amplitude could be a matter of smaller-amplitude AGWs in the lower thermosphere. In other words, fluid amplification is less, up to the lower thermosphere, than it is up to the thermosphere. If AGWs do reach the thermosphere, they could produce LSWS, around or after SS_E, through a neutral-ion coupling process that involves the *F*-region Pedersen current (Klostermeyer 1978).

Studies seeking correlation between convective activity and ESF, however, have produced mixed results (McClure et al. 1998; Su et al. 2008; Tsunoda 2010a,b,c). Correlation was best in the South American sector (Tsunoda 2010c). It turns out that the ESF patches over Jicamarca on the night of 28 to 29 August 2012 were, in fact, associated with deep convective activity in the troposphere. To illustrate, we present four maps of outgoing longwave radiation (OLR), for the Peruvian sector, in Figure 9. Following Waliser et al. (1993), we can interpret a localized blue-colored region as an MCC. The OLR maps were taken every 30 min. Other than that one region, where there may be two MCCs next to each other, the entire area

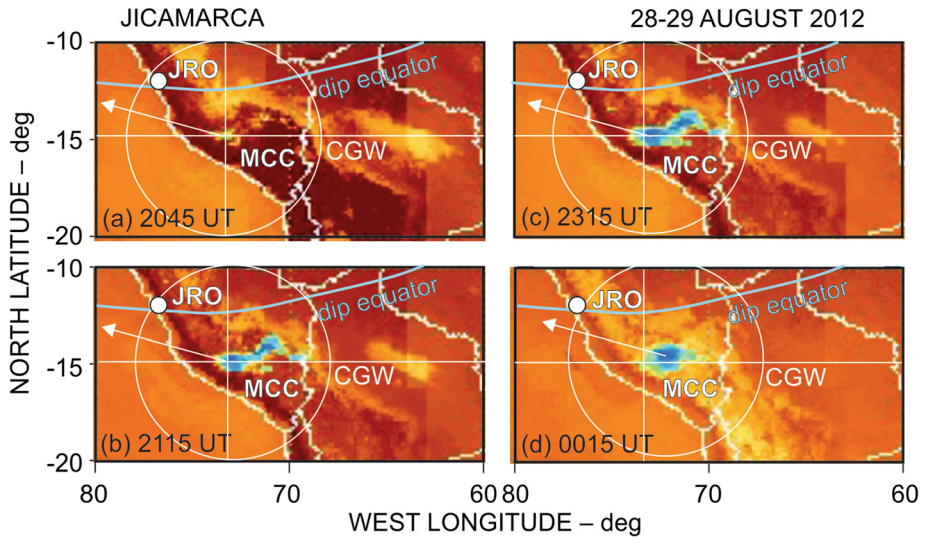

Figure 9 OLR maps showing the temporal development of a MCC (blue colored) region near JRO on 28-29 August 2012. (a) 2045 UT: very weak MCC. **(b)** 2115 UT: appearance of an extended region of deep convection. **(c)** 2315 UT: sustained convective activity. **(d)** 0015 UT: change in shape of MCC.

was devoid of convective activity. This event took place during the southern winter period, when both convective activity and strong PSSR rates are rare (Tsunoda 2010c). Prior to 2045 UT on August 28, MCCs were not detected. Activity intensified around 2115 UT and continued through 0015 UT on August 29.

The geometry appears to be ideal for neutral-ion coupling; that is, the MCC was located about 600 km (white circle) to the east-southeast of the Jicamarca Radio Observatory (JRO). Given the localized nature of the MCC, we envision that circular AGWs (CGWs) were excited (Tsunoda 2010b). Westward-propagating CGWs are most likely to penetrate to the thermosphere in the presence of an eastward U (e.g., Vadas 2007; Fritts and Vadas 2008). Moreover, neutral-ion coupling is expected to be most efficient, when the CGW phase front is aligned with B. Hence, we anticipate that the AGW reached F-region altitude in the direction of the white arrow, to the west of JRO. And, according to Waldock and Jones (1987), the source region in the troposphere is likely located between 250 and 1,500 km from the observed ionospheric perturbations. The ESF patches that arrived from the west of JRO are consistent with this scenario.

It is important to keep in mind that an AGW propagates relative to the background neutral gas. If the neutral gas moves relative to the ground reference frame (i.e., U), the phase velocity of a westward-propagating AGW will be Doppler-shifted to a value that is the difference of the two velocities. An extended interaction time for the neutral-ion coupling process, often referred to as 'spatial resonance' (Whitehead 1971), is possible when this difference velocity is matched with the zonal transport of the bottomside F layer. It turns out that LSWS is either nearly stationary, or drifts slowly westward, during the early stages of the growth phase (Tsunoda and White 1981; Kudeki et al. 1981; Tsunoda 2005, 2007; Tsunoda et al. 1981, 2013), when E-region dynamo still exerts control. The drift direction of upwellings becomes eastward during the structure phase (e.g., see Figure 6), when the F-region dynamo prevails. More details regarding this kind of geometry for spatial resonance can be found in Tsunoda (2007).

Growth phase

There are three features of interest that appear during the growth phase: (1) amplification of upwellings, (2) appearance of small-scale irregularities along the west wall of upwellings, and (3) the absence of EPBs. The first two, taken together, appear consistent with the notion that they are produced by the interchange instability, driven by orthogonal forces. That is, upwelling amplification could result from the interchange instability driven by the eastward electric field (E) that is responsible for the PSSR (gravity is likely a lesser player because the altitude of the bottomside F layer is, at this time, still relatively low). Backscatter along the west wall could be produced by the interchange instability driven by an eastward U.

Absence of EPBs in the presence of the other two features, however, calls for some discussion. A reasonable explanation might be velocity-shear effects. Without

velocity shear, the growth rate of the interchange instability should be larger for smaller-scale structures ($kL >> 1$) than for larger-scale structures ($kL \leq 1$); for example, see Guzdar et al. (1982, 1983), their Figure 1 (here, k is the wavenumber for LSWS, and L is the scale length for the velocity shear). However, in the presence of velocity shear, the growth rate of the interchange instability, for small-scale structures, should be strongly damped (Perkins and Doles 1975). Although the growth rate of larger-scale structures is not enhanced by velocity shear, it is less damped than that for the smaller-scale irregularities (Guzdar et al. 1982, 1983; Huba et al. 1983; Satyanarayana et al. 1984). This filtering process produces a relative maximum at a larger wavelength. Indeed, if we use 40 km as a reasonable estimate for the width of EPBs, and 400 km as that of upwellings, we would have a difference is spatial scale that is an order of magnitude.

A question that remains, is why do we observe small-scale irregularities (< few km) along the west wall of an upwelling, at a time when EPBs appear to be suppressed? One possibility is that the vector direction of the Pedersen current may have been close to tangent to isodensity contours. In this case, there is no velocity shear and the largest growth rate would be associated with small-scale irregularities. But, then, why don't we see secondary EPBs? There are other possible interpretations, which are beyond the scope of this paper. For example, (1) the spatial spectrum of seed plasma perturbations may have a peculiar distribution, (2) there is the question of which AGWs are capable of reaching *F*-region altitudes, and (3) there is the question of how the properties of LSWS will be colored by neutral-ion coupling. For our purposes here, we are mainly concerned with growth of upwellings, and how their presence controls the properties of ESF patches and clusters of EPBs. Amplification of upwellings during PSSR is a key process because the larger-amplitude upwellings profoundly distort the background conditions that must prevail in the absence of upwellings. In other words, upwelling growth transforms the background into a two-dimensional problem.

Onset phase

The appearance of the primary EPB from the crest of an upwelling argues in favor of curvature acting as an enhancement of the 'seed' amplitude. The implication is that the growth rate of the interchange instability is not large enough to produce EPBs from small-amplitude LSWS. Keeping in mind that upwelling amplitudes can reach 50 km without any appearance of an EPB, we can infer that either seed amplitude for EPBs is smaller than that for an upwelling, or that the growth rate of EPBs is smaller than that for an upwelling during PSSR. Furthermore, the confinement of the primary EPB to the vicinity of the crest of the upwelling, at the end of the PSSR, points to a likelihood that the conditions at the crest, created by upwelling growth, are responsible for the appearance of the primary EPB (Tsunoda 2005). It seems evident that curvature in isodensity contours in the vicinity of the crest will determine the seed amplitude for the primary EPB; ν_{in} should also be lowest at the crest. Both play roles in the interchange instability process.

Structure phase

In 'Structure phase: clustering and EW asymmetry' section, we showed how EPB clusters form, from EPB generation along the west wall, followed by the filling in of the entire upwelling region. Interpretation of west-wall structuring via the interchange instability, driven by an eastward U, appears straightforward. We also showed how EPBs move eastward relative to the upwelling, which leads to the filling of the entire upwelling region with EPBs, as can be seen in Figures 4 and 7. This latter behavior can be explained by the presence of velocity shear near the base of the F layer, where LSWS forms. As mentioned above, zonal drift, around SS_E, is likely controlled by the E-region dynamo at lower altitudes, and by the F-region dynamo at higher altitudes. In this case, plasma drift would be westward (eastward) at lower (higher) altitudes. It turns out that the isodensity contours, on which LSWS is observed, have been found to be either stationary or to drift slowly westward (Tsunoda and White 1981; Tsunoda et al. 2013). After SS_E, we expect control by the E-region dynamo to shift to lower altitudes, which means LSWS should begin to drift eastward as it falls under the control of the F-region dynamo. Nonetheless, the zonal drift speed of LSWS, which is often identified by the 10^5 el/cm^3 isodensity contour (see Figures 1 and 5a), will continue to move more slowly than plasma near the F-region peak, where N should be closer to 10^6 el/cm^3 (e.g., Zalesak et al. 1982). Hence, when EPBs penetrate upward into the F layer, they will drift with the background plasma because vertically elongated structures cannot develop a strong vertical polarization E. Hence, filling of upwellings with EPBs through relative zonal transport is expected.

EW asymmetry

It is not difficult to show that the EW asymmetry that develops within an upwelling is likely responsible for the asymmetries found in ESF patches and swoopers. To illustrate, we present a sketch in Figure 10 that illustrates what likely happens to paths of radio signals, when an upwelling with plasma structure is situated to the west of an ionosonde, and when the same structure is situated to the east of the station. To the west, rays can find surfaces of reflection along the west wall of the

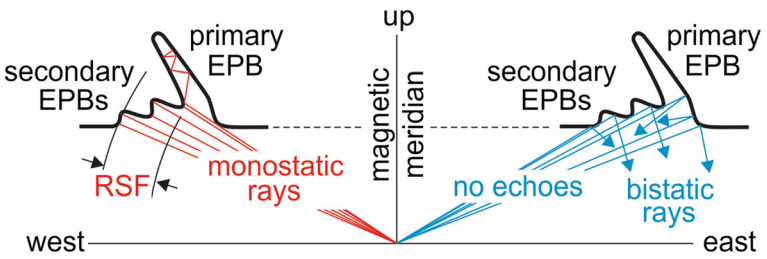

Figure 10 Sketch to illustrate the source of EW asymmetry in patches. Monostatic (red) rays return to ionosonde; bistatic (blue) rays do not return to ionosonde.

upwelling (where the bottomside shape of secondary EPBs are encountered) that will allow the rays to return to the ionosonde (see Thampi et al. (2012) for further discussion). We refer to these rays as monostatic rays; they are drawn with red lines. The extent of RSF would be related to the distribution of structure along the west wall. There is evidence that a ray could find its way into the primary EPB (or even secondary EPBs), as sketched (e.g., Tsunoda et al. 1995; Sales et al. 1996). Because the width of the EPB wedge (Tsunoda et al. 1982) decreases with altitude, up to the peak of the *F* layer, there is a good chance that the ray can retrace its way back to the ionosonde. This reflection mode is essentially identical to that described in Tsunoda (2012) to explain one form of MRE. To the east, the geometry is such that the rays can only skim the isodensity contours along the west wall (i.e., secondary EPBs), and when they do, the reflected paths are generally away from the ionosonde. We refer to rays that do not return to the ionosonde as bistatic rays, shown here with blue lines. This interpretation is consistent with the observations presented in Figure 3.

The sketch in Figure 10 can also be used to visualize how EW asymmetry manifests itself in swoopers and off-great-circle paths in TEP experiments. In the case of a short baseline (e.g., Davies and Chang 1968), we can treat the monostatic rays as those transmitted from one location, that encounter side reflections, but still reach the receiver at the other end of the bistatic path. This conversion is relatively simple because plasma structures are all expected to be elongated along *B* lines. In the case of long baselines, which are aligned more or less with the magnetic meridian, the simplest interpretation would be in terms of rays that follow a great-circle path in a direction away from the magnetic meridian, up to the vicinity of the dip equator. The one-hop path that is envisioned to straddle the dip equator is essentially the one just described for a short baseline. After side reflections have occurred, the remaining distance is envisioned to follow a great-circle path to the receiver (this is the geometry used by Röttger (1973) to interpret his TEP results).

Conclusions

From our perspective, the notion that an ESF patch or EPB cluster can be envisioned as a unit of disturbance is appealing. With hindsight, use of the term 'convective ionospheric substorm' does not seem to be so far-fetched. The spatial scale of the substorm is set by the zonal width of the upwelling, which is, perhaps typically, 400 km (e.g., Röttger 1973). The substorm process, which consists of three phases, is completed in one to two (or a few) hours. All of the pertinent electrodynamics take place in a plane transverse to *B*, with allowance for the mapping of *E* along *B*. With this framework for understanding, we are forced to keep in mind that even in the simplest of descriptions, ESF must be considered in terms of a two-dimensional (2D) structure (in plane transverse to *B*) that evolves with time. For example, it should be evident, from Figure 6, that an altitude-time-intensity description of ESF obtained with a fixed-beam radar (e.g., Woodman and La Hoz 1976) does not capture a true representation of the process.

The importance of a 2D description should be abundantly clear. The envisioned ESF process is still closely associated with the PSSR, which is consistent with most observations (e.g., Fejer et al. 1999). The primary EPBs, for example, are likely direct products of a strong PSSR and a high *F* layer, which is conducive to the gravitational interchange instability. The PSSR plays a less-direct role in the development of ESF patches and EPB clusters. That is, the PSSR amplifies an upwelling, and it is the zonal gradient along the west wall of the upwelling, together with an eastward *U*, that leads to the development of a cluster of secondary EPBs. Moreover, structuring of the west wall (but not east wall) is responsible for the EW asymmetry in numerous observations.

The finding that the ESF patches and EPB clusters tend to have spatial scales around 400 km is also appealing because most of the proposed physics appear to favor this spatial scale. The amplification of LSWS, but not EPBs, suggests that velocity shear may be responsible for a preferred larger wavelength (Guzdar et al. 1982, 1983). On the other hand, the observations (although still few) of LSWS prior to SS_E suggests that

the source is not the velocity shear in the bottomside *F* layer. If true, the source may be an AGW that is excited in the troposphere. It turns out that AGWs with larger spatial scales have higher phase velocities, which are more likely to survive the journey from troposphere to ionosphere (e.g., Vadas 2007). Once the AGW reaches the *F*-region, LSWS must be produced by AGWs through some form of neutral-ion coupling, which likely involves a polarization *E* (e.g., Klostermeyer 1978). It also turns out that most of the geometries that allow avoidance of polarization-shorting effects, such as the azimuth of propagation for AGWs (Tsunoda 2010a,c), AGWs have circular phase fronts (Tsunoda 2010b), and the presence of a conducting *E* layer on *B* lines that thread the phase fronts of AGWs, favor larger spatial scales.

In closing, our paradigm appears to be a reasonable first step toward constructing a unified working model for ESF. The model, as described, is likely more relevant to conditions of high solar activity during ESF season. Much remains to be done. There are already a significant number of observations that may not appear to fit the paradigm described in this paper. We suggest that care be taken in how one-dimensional descriptions are extrapolated to produce a 2D description, before drawing conclusions. That aside, it is likely that other interpretations will be needed to modify this working model to accommodate new observations, and to extend our understanding of the underlying physics.

Abbreviations

2D: two dimensional; AE-E: atmospheric explorer-E; AGW: atmospheric gravity wave; *B*: geomagnetic field; C/NOFS: communication/navigation outage forecasting system; CGW: circular AGW; CW: continuous wave; DLAT: dip latitude; *E*: electric field; EPB: equatorial plasma bubble; ESF: equatorial spread F; EW: east-west; GLAT: geographic latitude; GLON: geographic longitude; h'F: minimum virtual height of F layer; IS: incoherent scatter; JRO: Jicamarca radio observatory; LST: local solar time; LSWS: large-scale wave structure; MCC: mesoscale convective complex; MRE: multi-reflected echoes; N: plasma density; N_i: ion density; OLR: outgoing longwave radiation; PSSR: post-sunset rise; RSF: range spread F; SS_E: sunset in E-region; SS_F: sunset in F-region; ST: satellite trace; TEC: total electron content; TEP: transequatorial propagation; *U*: neutral wind; UT: universal time; ν_{in}: ion-neutral collision frequency.

Competing interests

The authors' declared that they have no competing interests.

Acknowledgements

Research was supported by the National Science Foundation under grant ATM-1242815, and the Air Force Office of Scientific Research, under Contract FA9550-15-C-0018. Ionograms from the Jicamarca Digisonde are available from website, umlcar.uml.edu/DIDBase/, operated by the University of Massachusetts, Lowell, Mass. The Digisonde is operated by the Jicamarca Radio Observatory. OLR maps are available from website, aviationweather.gov/obs/sat/intl/. The JpGU classification for this paper is space and planetary sciences.

Received: 8 November 2014 Accepted: 10 March 2015
Published online: 23 April 2015

References

Aarons J, Buchau J, Basu S, McClure JP (1978) The localized origin of equatorial *F* region irregularity patches. J Geophys Res 83:1659–1664

Abdu MA, Batista IS, Bittencourt JA (1981) Some characteristics of spread *F* at the magnetic equatorial station Fortaleza. J Geophys Res 86:6836–6842

Bernhardt PA, Siefring CL (2006) New satellite-based systems for ionospheric tomography and scintillation region imaging. Radio Sci 41:RS5S23, doi:10.1029/2005RS003360

Calvert W, Cohen R (1961) The interpretation and synthesis of certain spread *F* configurations appearing on equatorial ionograms. J Geophys Res 66:3125–3140

Calvert W, Davies K, Stiltner E, Brown JT (1963) Equatorial spread-*F* motions. In: Proc Intl Conf Ionosphere. Inst. Phys. Physical Soc, London, pp 316–322

Clemesha BR (1964) An investigation of the irregularities in the *F* region associated with equatorial type spread *F*. J Atmos Terr Phys 26:91–112

Clemesha BR, Wright RWH (1966) A survey of equatorial spread *F*. In: Newman P (ed) Spread F and Its Effects Upon Radio Wave Propagation and Communications. Agardograph 95, 3, W. and J. MacKay and Co., Ltd, London, England

Cohen R, Bowles KL (1961) On the nature of equatorial spread *F*. J Geophys Res 66:1081–1106

Davies K, Barghausen AF (1966) The effect of spread *F* on the propagation of radiowaves near the equator. In: Spread F and its Effects upon Radiowave Propagation and Communication, Chapter 2-13. Agardograph 95, Technivision, Maidenhead, England, pp 437–466

Davies K, Chang NJF (1968) Radio-Doppler observations of the ionosphere near the magnetic equator. In Scatter Propagation of Radio Waves, Part II, AGARD Conf. Proc. No. 37, Paper 52.

De la Beaujardiere O, Jeong L, Basu B, Basu S, Beach T, Bernhardt P, Burke W, Groves K, Heelis R, Holzworth R, Huang C, Hunton D, Kelley M, Pfaff R, Retterer J, Rich F, Starks M, Straus P, Valladares C (2004) C/NOFS: A mission to forecast scintillations. J Atmos Solar-Terr Phys 66:1573–1591

Dungey JW (1956) Convective diffusion in the equatorial *F* region. J Atmos Terr Phys 9:304–310

Farley DT, Balsley BB, Woodman RF, McClure JP (1970) Equatorial spread *F*: Implications of VHF radar observations. J Geophys Res 75:7199–7216

Fejer BG, Scherliess L, de Paula ER (1999) Effects of the vertical plasma drift velocity on the generation and evolution of equatorial spread *F*. J Geophys Res 104:19,859–19,869

Fritts DC, Vadas SL (2008) Gravity wave penetration into the thermosphere: Sensitivity to solar cycle variations and mean winds. Ann Geophys 26:3841–3861

Guzdar PN, Satyanarayana P, Huba JD, Ossakow SL (1982) Influence of velocity shear on the Rayleigh-Taylor instability. Geophys Res Lett 9:547–550

Guzdar PN, Satyanarayana P, Huba JD, Ossakow SL (1983) Correction. Geophys Res Lett 10:492

Hei MA, Heelis RA, McClure JP (2005) Seasonal and longitudinal variation of large-scale topside equatorial plasma depletions. J Geophys Res 110:A12315, doi:10.1029/2005JA011153

Huba JD, Ossakow SL, Satyanarayana P, Guzdar PN (1983) Linear theory of the E x B instability with an inhomogeneous electric field. J Geophys Res 88:425–434

Hysell DL, Kelley MC (1997) Decaying equatorial *F* region plasma depletions. J Geophys Res 102:20,007–20,017

Kelleher RF, Röttger J (1973) Equatorial spread *F* irregularities observed at Nairobi and on the transequatorial path Lindau-Tsumeb. J Atmos Terr Phys 35:1207–1211

Kelleher RF, Skinner NJ (1971) Studies of *F* region irregularities at Nairobi, II. By direct backscatter at 27.8 MHz. Ann Geophys 27:195–200

Kelley MC, de la Beaujardiere O, Retterer J, Makela JJ (2005) Introduction to special section on Communication/Navigation Forecasting System: A next step in Space Weather. Space Wea 3:S12C01, doi:10.1029/2005SW000189

Kelley MC, Rodrigues FS, Makela JJ, Tsunoda R, Roddy PA, Hunton DE, Retterer JM, de La Beaujardiere O, de Paula ER, Ilma RR (2009) C/NOFS and radar observations during a convective ionospheric storm event over South America. Geophys Res Lett 36:L00C07, doi:10.1029/2009GL039378

Kelley MC, Makela JJ, de La Beaujardiere O, Retterer J (2011) Convective ionospheric storms: A review. Rev Geophys 49:RG2003, doi:10.1029/2010RG000340

Kil H, Heelis RA (1998a) Global distribution of density irregularities in the equatorial ionosphere. J Geophys Res 103:407–417

Kil H, Heelis RA (1998b) Equatorial density irregularity structures at intermediate scales and their temporal evolution. J Geophys Res 103:3969–3981

Klostermeyer J (1978) Nonlinear investigation of the spatial resonance effect in the nighttime equatorial *F* region. J Geophys Res 83:3753–3760

Kudeki E, Fejer BG, Farley DT, Ierkic HM (1981) Interferometer studies of equatorial *F*-region irregularities and drifts. Geophys Res Lett 8:377–380

Makela JJ, Kelley MC, Su S-Y (2005) Simultaneous observations of convective ionospheric storms: ROCSAT-1 and ground-based imagers. Space Wea 3: S12C02

Makela JJ, Kelley MC, De La Beaujardiere O (2006) Convective ionospheric storms: A major space weather problem. Space Wea 4. doi:10.1029/2005SW000145.
Maruyama T, Kawamura M (2006) Equatorial ionospheric disturbance observed through a transequatorial HF propagation experiment. Ann Geophys 24:1401–1409
McClure JP, Hanson WB, Hoffman JH (1977) Plasma bubbles and irregularities in the equatorial ionosphere. J Geophys Res 82:2650–2656
McClure JP, Singh S, Bamgboye DK, Johnson FS, Kil H (1998) Occurrence of equatorial *F* region irregularities: Evidence for tropospheric seeding. J Geophys Res 103:29,119–29,135
Nielson DL, Crochet M (1974) Ionospheric propagation of HF and VHF radio waves across the geomagnetic equator. Rev Geophys Space Phys 12:688–702
Perkins FW (1975) Doles JH III. Velocity shear and the E x B instability J Geophys Res 80:211–214
Röttger J (1973) Wave-like structures of large-scale equatorial spread-*F* irregularities. J Atmos Terr Phys 35:1195–1206
Saito S, Maruyama T, Ishii M, Kubota M, Ma G, Chen Y, Li J, Duyen CH, Truong TL (2008) Observations of small- to large-scale ionospheric irregularities associated with plasma bubbles with a transequatorial HF propagation experiment and spaced GPS receivers. J Geophys Res 113:A12313, doi:10.1029/2008JA013149
Sales GS, Reinisch BW, Scali JL, Dozois C, Bullett TW, Weber EJ, Ning P (1996) Spread *F* and the structure of equatorial ionization depletions in the southern anomaly region. J Geophys Res 101:26,819–26,827
Satyanarayana P, Guzdar PN, Huba JD, Ossakow SL (1984) Rayleigh-Taylor instability in the presence of a stratified shear layer. J Geophys Res 89:2945–2954
Singh S, Johnson FS, Power RA (1997) Gravity wave seeding of equatorial plasma bubbles. J Geophys Res 102:7399–7410
Su SY, Chao CK, Liu CH (2008) On monthly/seasonal/longitudinal variations of equatorial irregularity occurrences and their relationship with the postsunset vertical drift velocities. J Geophys Res 113:A05307, doi:10.1029/2007JA012809
Thampi SV, Yamamoto M, Tsunoda RT, Otsuka Y, Tsugawa T, Uemoto J, Ishii M (2009) First observations of large-scale wave structure and equatorial spread *F* using CERTO radio beacon on the C/NOFS satellite. Geophys Res Lett 36: L18111, doi:10.1029/2009GL039887
Thampi SV, Tsunoda R, Jose L, Pant TK (2012) Ionogram signatures of large-scale wave structure and their relation to equatorial spread *F*. J Geophys Res 117: A08314, doi:10.1029/2012JA017592
Tsunoda RT (1981) Time evolution and dynamics of equatorial backscatter plumes, 1, Growth phase. J Geophys Res 86:139–149
Tsunoda RT (1983) On the generation and growth of equatorial backscatter plumes. 2. Structuring of the west walls of upwellings. J Geophys Res 88:4869–4874
Tsunoda RT (2005) On the enigma of day-to-day variability in equatorial spread *F*. Geophys Res Lett 32:L08103, doi:10.1029/2005GL022512
Tsunoda RT (2007) Seeding of equatorial plasma bubbles with electric fields from an E_s-layer instability. J Geophys Res 112:A06304, doi:10.1029/2006JA012103
Tsunoda RT (2008) Satellite traces: An ionogram signature for large-scale wave structure and a precursor for equatorial spread *F*. Geophys Res Lett 35: L20110, doi:10.1029/2008GL035706
Tsunoda RT (2009) Multi-reflected echoes: Another ionogram signature of large-scale wave structure. Geophys Res Lett 36:L01102, doi:10.1029/2008GL036221
Tsunoda RT (2010a) On seeding equatorial spread *F* during solstices. Geophys Res Lett 37:L05102, doi:10.1029/2010GL042576
Tsunoda RT (2010b) On seeding equatorial spread *F*: Circular gravity waves. Geophys Res Lett 37:L10104, doi:10.1029/2010GL043422
Tsunoda RT (2010c) On equatorial spread *F*: Establishing a seeding hypothesis. J Geophys Res 115:A12303, doi:10.1029/2010JA015564
Tsunoda RT (2012) A simple model to relate ionogram signatures to large-scale wave structure. Geophys Res Lett 39:L18107, doi:10.1029/2012GL053179
Tsunoda RT, White BR (1981) On the generation and growth of equatorial backscatter plumes—1. Wave structure in the bottomside F layer J Geophys Res 86:3610–3616
Tsunoda RT, Baron MJ, Owen J, Towle DM (1979) ALTAIR: An incoherent scatter radar for equatorial spread *F* studies. Radio Sci 14:1111–1119
Tsunoda RT, Livingston RC, McClure JP, Hanson WB (1982) Equatorial plasma bubbles: Vertically elongated wedges from the bottomside *F* layer. J Geophys Res 87:9171–9180
Tsunoda RT, Livingston RC, Buonocore JJ, McKinley AV (1995) The frequency-agile radar: A multifunctional approach to remote sensing of the ionosphere. Radio Sci 30:1623–1643
Tsunoda RT, Bubenik DM, Thampi SV, Yamamoto M (2010) On large-scale wave structure and equatorial spread *F* without a post-sunset rise of the *F* layer. Geophys Res Lett 37:L07105, doi:10.1029/2009GL042357
Tsunoda RT, Yamamoto M, Tsugawa T, Hoang TL, Tulasi Ram S, Thampi SV, Chau HD, Nagatsuma T (2011) On seeding, large-scale wave structure, equatorial spread *F*, and scintillations over Vietnam. Geophys Res Lett 38:L20102, doi:10.1029/2011GL049173
Tsunoda RT, Thampi SV, Nguyen TT, Yamamoto M (2013) On validating the relationship of ionogram signatures to large-scale wave structure. J Atmos Solar-Terr Phys 103:30–35
Tsunoda RT, Nguyen TT, Le MH (2015) Effects of tidal forcing, conductivity gradient, and active seeding, on the climatology of equatorial spread *F* over Kwajalein. J Geophys Res 120. doi:10.1002/2014JA020762.
Tulasi Ram S, Yamamoto M, Tsunoda RT, Thampi SV (2012) On the application of differential phase measurements to study the zonal large scale wave structure (LSWS) in the ionospheric electron content. Radio Sci 47:RS2001, doi:10.1029/2011RS004870
Tulasi Ram S, Yamamoto M, Tsunoda RT, Chau HD, Hoang TL, Damtie B, Wassaie M, Yatini CY, Manik T, Tsugawa T (2014) Characteristics of large-scale wave structure observed from African and Southeast Asian longitude sectors. J Geophys Res 119. doi:10.1002/2013JA019712.
Vadas SL (2007) Horizontal and vertical propagation and dissipation of gravity waves in the thermosphere from lower atmospheric and thermospheric sources. J Geophys Res 112:A06305, doi:10.1029/2006JA011845
Waldock JA, Jones TB (1987) Source regions of medium scale travelling ionospheric disturbances observed at mid-latitudes. J Atmos Terr Phys 49:105–114
Waliser DE, Graham NE, Gautier C (1993) Comparison of the highly reflective cloud and outgoing longwave radiation datasets for use in estimating tropical deep convection. J Climate 6:331–353
Weber EJ, Buchau J, Eather RH, Mende SB (1978) North-south aligned equatorial airglow depletions. J Geophys Res 83:712–716
Weber EJ, Buchau J, Moore JG (1980) Airborne studies of equatorial *F* layer ionospheric irregularities. J Geophys Res 85:4631–4641
Weber EJ, Brinton HC, Buchau J, Moore JG (1982) Coordinated airborne and satellite measurements of equatorial plasma depletions. J Geophys Res 87:10,503–10,513
Whitehead JD (1971) Ionization disturbances caused by gravity waves in the presence of an electrostatic field and a background wind. J Geophys Res 76:238–241
Woodman RF, La Hoz C (1976) Radar observations of *F* region equatorial irregularities. J Geophys Res 81:5447–5466
Yokoyama T, Fukao S, Yamamoto M (2004) Relationship of the onset of equatorial *F* region irregularities with the sunset terminator observed with the Equatorial Atmosphere Radar. Geophys Res Lett 31:L24804, doi:10.1029/2004GL021529
Zalesak ST, Ossakow SL, Chaturvedi PK (1982) Nonlinear equatorial spread *F*: The effect of neutral winds and background Pedersen conductivity. J Geophys Res 87:151–166